Supporting Information

Hollow Mo-doped NiS_x nanoarrays decorated with NiFe layered double-hydroxide for efficient and stable overall water splitting

Yanyan Li[a], Haoran Guo[a], Yao Zhang[a,b], Haotian Zhang[a], Jiayang Zhao[a], and Rui Song[a,*]

[a] School of Chemical Sciences, University of Chinese Academy of Sciences, 19 Yuquan Road, Shijingshan District, Beijing, 100049, PR China

[b]School of Materials and Chemical Engineering, Xuzhou University of Technology, Xuzhou 221018, P. R. China

*Email: rsong@ucas.ac.cn

目录

1. Experimental Section

1.1 Chemicals and Reagents

Ammonium molybdate tetrahydrate ($(NH_4)_6Mo_7O_{24}\cdot 4H_2O$), iridium dioxide ($IrO_2$) and Pt/C (20 wt%) are purchased from Shanghai Macklin Biochemical Industrial Co., Ltd. Iron nitrate nonahydrate (Fe $(NO_3)_3\cdot 9H_2O$), Sodium sulfide (Na_2S) and Nickel(II) nitrate hexahydrate ($Ni(NO_3)_2\cdot 6H_2O$) are purchased from Aladdin Industrial Co., Ltd. All chemicals are used as received without further purification. The deionized water (18.2 MΩ cm) is used throughout the whole experiments.

1.2 Synthesis of $NiMoO_4\cdot xH_2O$/NF

First, the commercial Ni foam (2 × 3 cm) was sonicated in acetone, ethanol, and water for each 15 min, then placed vertically into a 50 mL Teflon autoclave. Next, 15 mL of $Ni(NO_3)_2\cdot 6H_2O$ (0.04 M) and $(NH_4)_6Mo_7O_2\cdot 4H_2O$ (0.01 M) aqueous solution was transferred into the above Teflon autoclave. The autoclave was sealed and heated at 150 °C for 6 h in a drying oven to obtain $NiMoO_4\cdot xH_2O$ micro rods grown on Ni foam ($NiMoO_4\cdot xH_2O$/NF).

1.3 Synthesis of Mo-NiS_x/NF

The Mo-NiS_x/NF nanosheet arrays through a mild sulfur-modified corrosion method. Briefly, 300 mg $Na_2S\cdot 9H_2O$ was dissolved in 30 mL distilled water and transferred to a 50 mL beaker with the as-prepared $NiMoO_4\cdot xH_2O$/NF, maintained at 60℃ for 8 h. The obtained Mo-NiS_x/NF were rinsed with deionized water and ethanol several times and dried at 60 °C overnight.

1.4 Synthesis of Mo-NiS_x@NiFe LDH/NF

The highly dispersed NiFe LDH nanoparticles were electrodeposited onto the surface of the Mo-NiS_x/NF array to obtain Mo-NiS_x@NiFe LDH/NF. Electrodeposition was performed using a three-electrode configuration, with a Mo-NiS_x/NF electrode, carbon rod and Ag/AgCl electrode as working electrode, the counter electrode and reference electrode, respectively. To prepare the electrodeposition electrolyte, 150 μmol $Fe(NO_3)_3\cdot 9H_2O$ and 150 μmol $Ni(NO_3)_2\cdot 6H_2O$ were added into 50 mL deionized

water. The electrodeposition process was then performed fixing deposition potential at −1.0 V vs. Ag/AgCl for 3 min. Finally, the as-obtained electrodes were alternately rinsed with deionized water and ethanol several times, and dried in vacuum before use. For comparison, NiFe LDH electrode was prepared via direct electrodeposition of NiFe nanoparticles onto the pretreated Ni foam under the same procedure.

1.5 Synthesis of the Pt/C and IrO_2

For comparison, 5 mg of Pt/C (or IrO_2) and 50 μL of 5 wt% Nafion solution were dispersed in 950 μL of isopropyl alcohol by sonication for 1 h. Then the 320 μL homogeneous suspension was drop-cast onto carbon papers electrode where the total effective loading surface area of noble-metal catalysts was 0.5 × 0.5 × 2 cm^{-2}, and the mass loading was 1.7 mg cm^{-2}.

1.6 Electrode materials characterizations

1) Grazing incidence X-ray diffraction (XRD) was carried out on an X'Pert PRO PANanalytical instrument (Bragg-Brentano geometry with fixed divergence slits, position sensitive detector, continuous mode, room temperature, Cu Kα radiation).
2) Scanning electron microscopy (SEM) was carried out on a Hitachi SU8220. Transmission electron microscopy (TEM) and energy-dispersive X-ray spectroscopy (EDS) elemental mapping attached to the TEM was performed on a Tecnai G2 F20 S-TWIN TEM microscope operated at 200 kV.
3) Raman spectra were examined using a Renishaw Invia Raman spectrometer with a 532 nm laser source.
4) X-ray photoelectron spectra (XPS) were measured by a Thermo Scientific ECSA Lab 250Xi X-ray photoelectron spectrometer with an Al Kα X-ray radiation (1486 eV).
5) The contact angle of gas (air) bubbles on the electrode materials under water were measured by the captive bubble method using droplet shape analyzer DSA100, Germany.
6) Nitrogen absorption/desorption isotherms are measured on a Micromeritics ASAP2460 instrument and after the samples are degassed about 4 h at 100 °C and

the specific surface areas are calculated by the Brunauer-Emmett-Teller (BET) method.

1.7 Electrochemical Measurements

All the electrochemical measurements were conducted in a standard three-electrode setup on a CHI 660E electrochemical workstation (Chenhua Instruments, Shanghai, China). A H-cell with a glass frit separating the anodic and cathodic compartments was used (three-electrode configuration). The fabricated self-supported electrodes (1 × 0.5 cm) were directly employed as working electrodes, while a graphite rod and an Hg/HgO (filled in 1 M KOH) electrode as the counter electrode and the reference electrode, respectively. Before Multiple cyclic voltammetry (CV) scans were firstly performed at a scan rate of 5 mV s^{-1} until reached a stable state of electrodes. Then, linear sweep voltammetry (LSV) was conducted with a scan rate of 5 mV s^{-1} in 1 M KOH solution. The electrochemical impedance spectroscopy (EIS) measurements were carried out at an overpotential of 294 mV for the OER and 81 mV for the HER over a frequency range from 100 kHz to 0.01 Hz with an amplitude of 10 mV. The long-term stability was tested by chronopotentiometry. All the polarization curves were corrected using 85% *iR* compensation. Potentials were referenced to the reversible hydrogen electrode (RHE): *E* vs. RHE = *E* vs. Hg/HgO + 0.098 + 0.059 pH. The overpotential (η) was calculated according to the following equation: η = *E* vs. RHE - 1.23 V.

1.8 Calculation of ECSA

Based on the literature,[1] cyclic voltammetry (CV) was carried out in 1 M KOH to probe the electrochemical double-layer capacitance of the various samples at non-Faradic overpotentials to estimate the effective electrode surface areas. Accordingly, a series of CV measurements were performed at various scan rates (20, 40, 60, 80 and 100 mV s^{-1}) in 1.05-1.15 V vs. RHE range, and the sweep segments of the measurements were set to 10 to ensure consistency. By plotting the difference in current density (J) between the anodic and cathodic sweeps (J_{anodic} - $J_{cathodic}$) at 1.10 V vs. RHE against the scan rate, a linear trend was observed. The slope of the fitting line was found

to be equal-to-twice the geometric double-layer capacitance (C_{dl}), which was proportional to the effective electrode surface area of the materials. Therefore, the electrochemical surface areas of different samples can be compared with one another based on their C_{dl} values. However, it should be noted that this comparison makes sense only when the measurement of materials was carried out under the same condition.

The electrochemically active surface area (ECSA) was calculated from the C_{dl} value following the equations:[2]

$$ECSA = \frac{C_{dl}}{40\ \mu F\ cm^{-2}\ per\ cm^{2}_{ECSA}} \quad \text{(S1)}$$

1.9 Calculation of the turnover frequency (TOF)

The turnover frequency (TOF) is estimated by the following equation:[3]

$$TOF = \frac{|j| \times N_A}{m \times F \times n} \quad \text{(S2)}$$

where j is current density at defined overpotential; N_A denotes the Avogadro number; F is the Faraday constant, m is the number of the consumed electrons forming one H_2 or O_2 molecule from water. The number of surface active sites (n) can be calculated with the formula: $n = Q/(1\times1.602\times10^{-19})$, and assume a one-electron transfer process for both reduction and oxidation herein. While charge (Q) can be obtained from the reductive negative scan peak areas of cyclic voltammetry (CV) curves at a specific scan rate, for example 300 mV/s. Q can be obtained with the formula: Q = peak area/300 mV/s.

1.10 DFT calculation

First-principles calculations were performed within the density functional theory framework[4]. The projector-augmented wave (PAW) method[5, 6] and the generalized gradient approximation (GGA)[7] for the exchange-correlation energy functional, as implemented in the Vienna ab initio simulation package (VASP)[8-11] were used. The GGA calculation was performed with the Perdew-Burke-Ernzerhof (PBE)[12] exchange-correlation potential. Considered long-range interaction between

molecules/intermediates and surface, Van der Waals interactions were considered using DFT-D3 correlation.[13] A combined supercell slab model was built to simulate the surface of NiFe LDH and NiS_x. To avoid effects come from other slabs, a vacuum of 15 Å was added along z direction. The convergence criterion of geometry relaxation was set to 0.03 $eV \cdot Å^{-1}$ in force on each atom. The energy cutoff for plane wave-basis was set to 600 eV. The K points were sampled with 3×3×1 by Monkhorst-Pack method.

For OER, the Gibbs free energy was calculated by the generally reported four electrons process:

$$OH^- + * \rightarrow *OH + e^- \quad (S3)$$

$$OH^- + *OH \rightarrow *O + H_2O\ (l) \quad (S4)$$

$$*O + OH^- \rightarrow *OOH + e^- \quad (S5)$$

$$*OOH + OH^- \rightarrow O_2 + H_2O\ (l) + e^- \quad (S6)$$

Where * represents an adsorption site on the catalyst, and *OH, *O and *OOH denote the corresponding adsorbed intermediates. Also, at standard conditions, the free energies change for all OER electrochemical steps ($\Delta G_{1\text{-}4}$) can be expressed as:

$$\Delta G_1 = \Delta G_{*OH} \quad (S7)$$

$$\Delta G_2 = \Delta G_{*O} - \Delta G_{*OH} \quad (S8)$$

$$\Delta G_3 = \Delta G_{*OOH} - \Delta G_{*O} \quad (S9)$$

$$\Delta G_4 = 4.92 - \Delta G_{*OOH} \quad (S10)$$

Therefore, the theoretical overpotential η was obtained according to the equation:

$$\eta = \max [\Delta G_1, \Delta G_2, \Delta G_3, \Delta G_4]/e - 1.23\ V \quad (S11)$$

The change in free energy (ΔG) of per reaction step was calculated as following:[14]

$$\Delta G = \Delta E + \Delta ZPE - T \cdot \Delta S + \Delta G_U + \Delta G_{pH} \quad (S12)$$

Where ΔE is the change of the total reaction energy obtained from DFT calculation, ΔZPE is the change of the zero-point energy, T is the temperature (300K), and ΔS is the change of the entropy. $\Delta G_U = -eU$, where U is the potential at the electrode and e is the transferred charge. $\Delta G_{pH} = k_B \cdot T \times \ln 10 \times pH$, where k_B is the Boltzmann constant and T = 300 K. In this work, the influence of pH was neglected. The free energy of O_2 is obtained from the reaction $O_2 + 2H_2 \rightarrow 2H_2O$, which is 4.92 eV at 300 K and a pressure of 0.035 bar. The free energy of OH^- is defined as $G(H_2O)$-$G(H^+)$, and

the free energy of H^+ is equal to $1/2H_2$. The entropies of molecules (including O_2, H_2, and H_2O, etc.) in the gas (or liquid) phase are taken from the "CRC Handbook of Chemistry and Physics".[15]

For HER, the hydrogen adsorption free energy (ΔG_{H^*}) was calculated by the following equation:[16]

$$\Delta G_{H^*} = \Delta E_{H^*} + 0.24\ \text{eV} \quad \text{(S13)}$$

Where ΔE_{H^*} is defined by the following equation:

$$\Delta E_{H^*} = E_{H^*} - (E_* + 1/2E_{H_2}) \quad \text{(S14)}$$

Where E_{H^*} is the total energy of H atom on the support, E_* is the total energy of support, E_{H_2} is the energy of the gas H_2 calculated by setting the isolated H_2 in a box of 10.0 Å×10.0 Å×10.0 Å. The Gibbs free energy for the well-known highly efficient Pt catalyst is near-zero as $|\Delta G_{ads}| \approx 0.09$ eV.[17]

2. Results and discussion

2.1 Characterization of catalysts

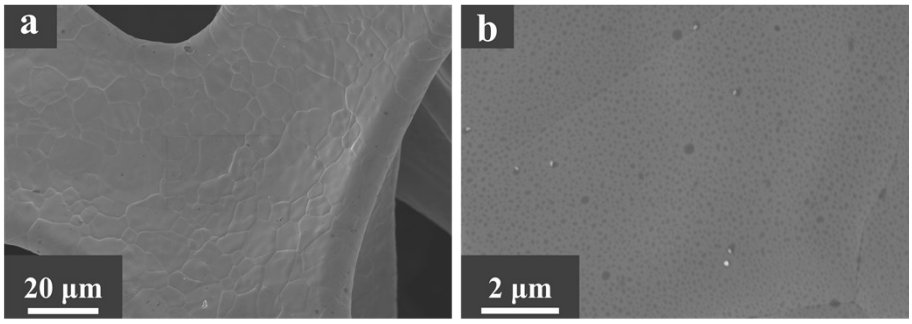

Fig. S1 SEM images of NF under different magnifications.

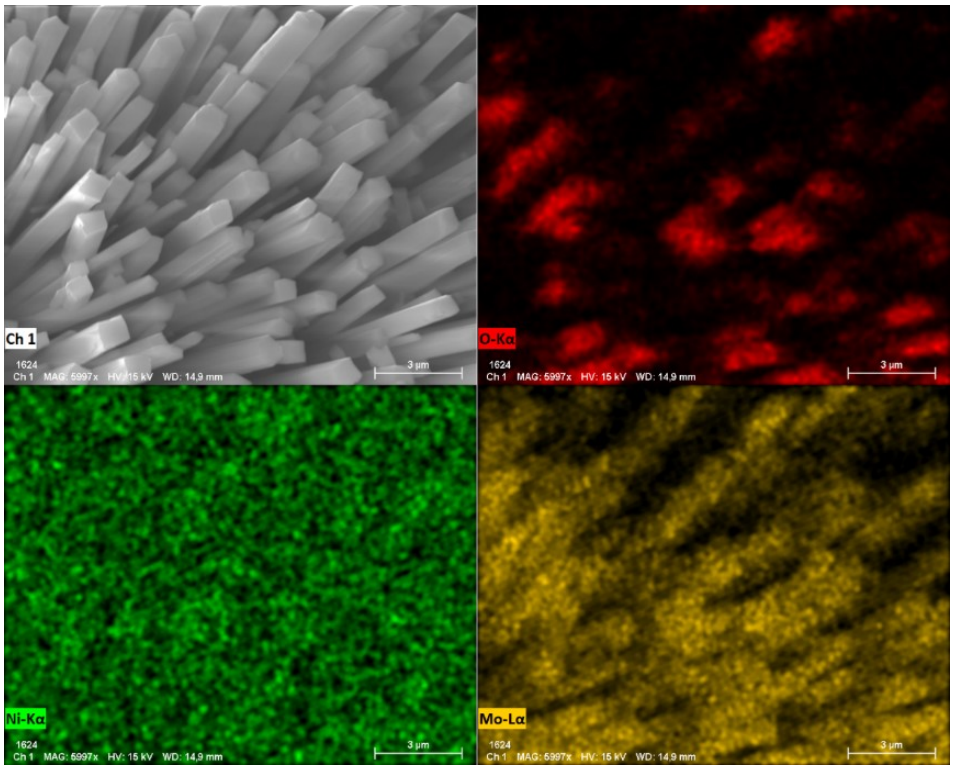

Fig. S2 SEM elemental mapping images of $NiMoO_4 \cdot xH_2O$/NF from the surface.

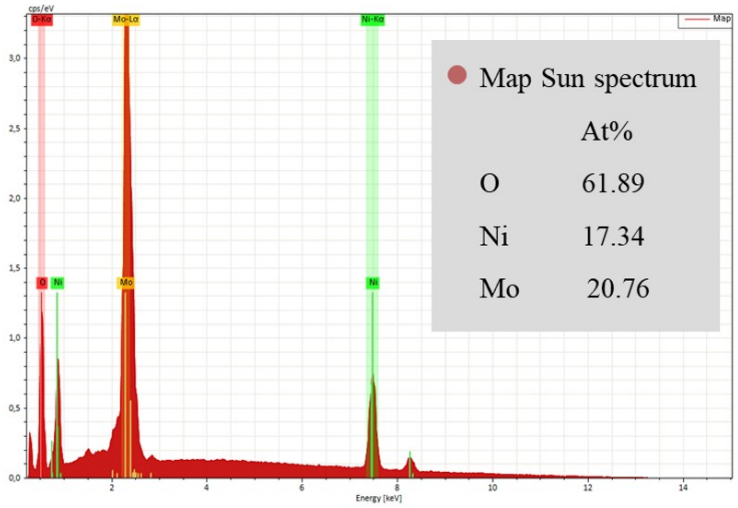

Fig. S3 EDS spectrum and the elemental content analysis of $NiMoO_4 \cdot xH_2O$/NF near substrate.

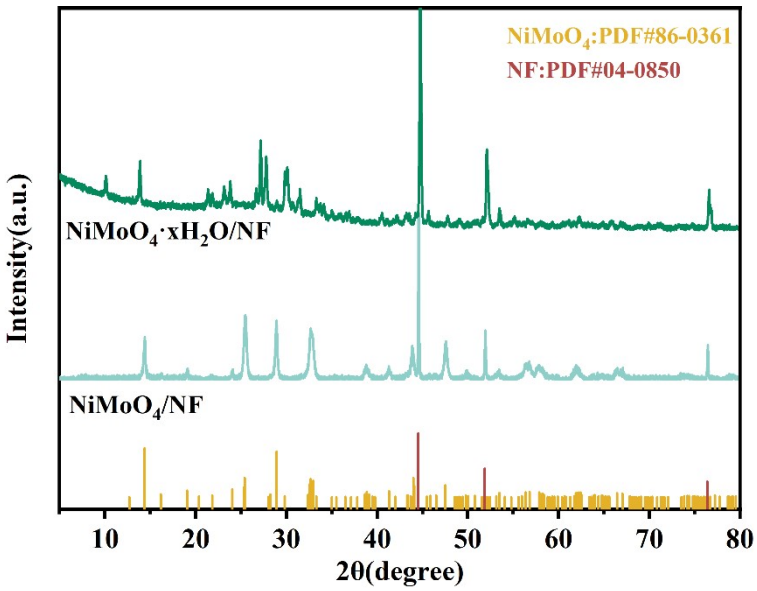

Fig. S4 XRD pattern of $NiMoO_4$/NF and $NiMoO_4 \cdot xH_2O$/NF.

The XRD pattern shows the characteristic diffraction peaks of metal Ni at 44.6° and 52.0° (JCPDS, No. 04-0850) and diffraction peaks of $NiMoO_4 \cdot xH_2O$ were also detected, which has been widely reported. Most of all, the $NiMoO_4 \cdot xH_2O$ microrods were reacted at 350 °C for 1 h under a vacuum to get $NiMoO_4$ /NF nanorods. All peaks of $NiMoO_4$/NF are matched well with the simulated patterns, suggesting the successful synthesis of $NiMoO_4 \cdot xH_2O$.

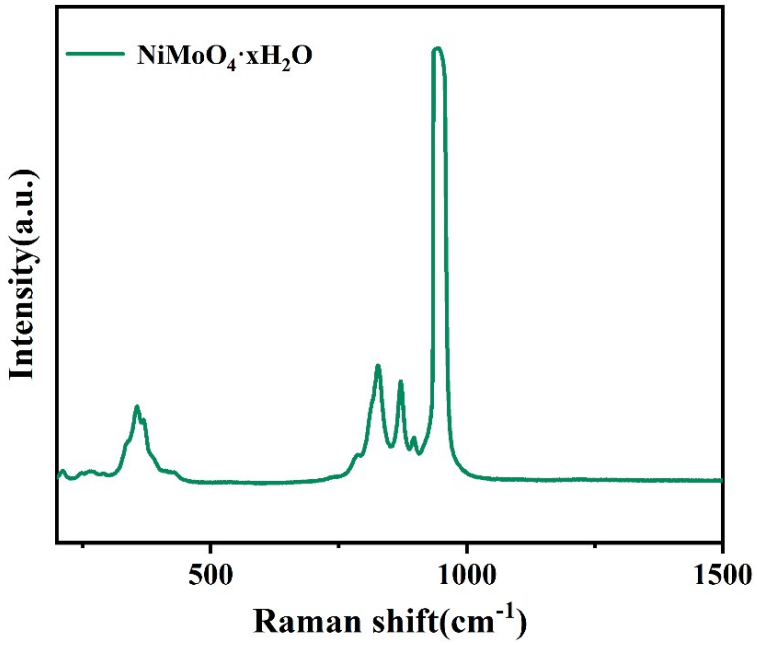

Fig. S5 Raman spectra of hydrated $NiMoO_4 \cdot xH_2O$/NF.

$NiMoO_4 \cdot xH_2O$ displays intense Raman peaks at 948, 870, and 830 cm^{-1}, with a broad peak at 358 cm^{-1}. The Raman band located at 948 cm^{-1} is correlated with the symmetric stretching mode of molybdenum and oxygen linkage. The bands at 870 cm^{-1} are assigned to the asymmetric stretching modes of the oxygen in the O-Mo-O bond. Most of the Raman peaks observed for the hydrous samples are consistent with those reported in the literature.[18]

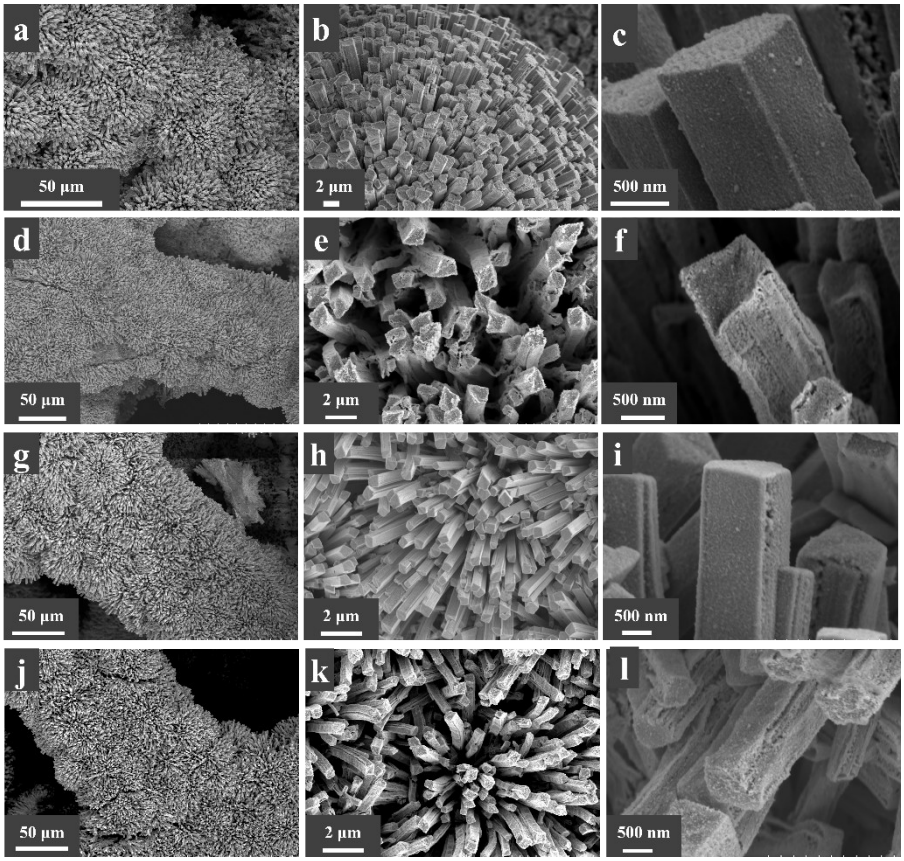

Fig. S6 SEM images of Mo-NiS_x/NF at different hydrothermal temperature hydrothermal temperature (**a, b, c**) 40 ℃/8h, (**c, d, e**) 80 ℃/8h, (**g, h, i)** 60 ℃/6h and (**j, k, l**) 60 ℃/10h under different magnifications.

The Mo-NiS_x/NF exhibits different morphologies (Fig. S6) depending on hydrothermal temperatures (i.e., 40, 60 and 80 ℃) and hydrothermal durations (i.e., 4, 6 and 8 h). The low hydrothermal temperatures (40 ℃) and duration of 8 h will result in the incomplete sulfidation of $NiMoO_4 \cdot xH_2O$/NF nanorods (Fig. S6a, b, c). Upon increasing hydrothermal temperature to 80 ℃ will lead to the destroy of the rod structure of the precursor (Fig. S6d, e, f). Next, the influence of hydrothermal time on Mo-NiS_x/NF morphology was investigated at 60℃. At 6 h, Mo-NiS_x/NF presents solid nanorods in a wide range (Fig. S6g, h, i). When extended to 10 h the nanorods present hollow but distorted shapes. Therefore, Mo-NiSx/NF obtained under the condition of vulcanization at 60℃ and 8 h was selected as the skeleton of subsequent electrodeposition.

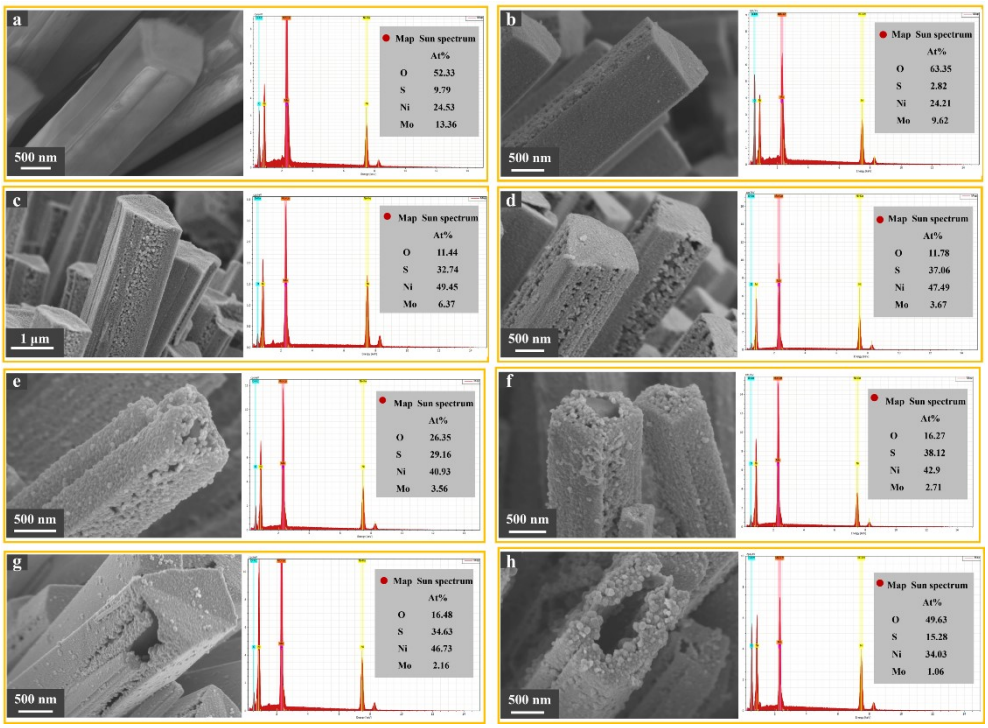

Fig. S7 SEM images and the elemental content analysis of Mo-NiSx/NF after different sulfidation times: **a)** 1 h, **b)** 2 h, **c)** 3 h, **d)** 4 h, **e)** 5 h, **f)** 6 h, **g)** 7 h and **h)** 8 h.

In order to further explore the mechanism for the formation of Mo-NiS_x@NiFe LDH/NF, the SEM images of Mo-NiS_x after different sulfidation times are tested in Fig. R9. After being placed into the oil bath and after sulfidation for 1 h, only a slightly etched on the surface of $NiMoO_4 \cdot xH_2O$ (Fig. S7a). After treatment for 4 h, the Mo-NiS_x crystals with interconnected nanosheets grows around the periphery of the nanorods (Fig. S7b-d), the original 3D nanorod arrays of $NiMoO_4$ could be clearly found. As the reaction time increased to 8h (Fig. S7e-h), more dense crystals were synthesized, meanwhile un-sulfidated $NiMoO_4 \cdot xH_2O$ was basically invisible. Of note, the process is accompanied by the leaching of the Mo element, which can be seen from the element content of each time period. Specifically, at the beginning of the vulcanization process, sulfur ions (S^{2-}, from sodium sulfide) diffuse to the surface of NiMo precursor. Because of the outward diffusion rate of Ni/Mo ions is faster than the inward diffusion rate of S ions due to the smaller ionic radii of Ni/Mo ions, many fine holes are formed in the precursor.[19] As the reaction progresses, the holes grow together, eventually forming a hollow structured known as the Kirkendall Effect.[20] During this transfer, sulfur ions rarely form polymetallic sulfides with more than two metals (except $NiCo_2S_4$) due to

sulfur is less electronegative than oxygen.[21] At the same time, although Ni-Mo sulfide or molybdenum sulfide may be produced during the vulcanization process, they are unstable intermediates compared to NiS_x, resulting in their re-dissolution in reactions. As a result, an amount of molybdenum is leached during the Kendall effect, and a few of them in the form of substitution by Ni and forms Mo-S bonds for doping.

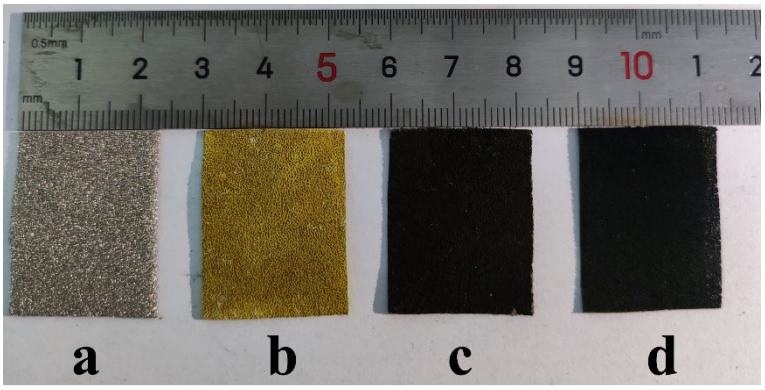

Fig. S8 Photographs of **a)** NF, **b)** $NiMoO_4 \cdot xH_2O$/NF, **c)** Mo-NiS_x/NF and **d)** Mo-NiS_x@NiFe LDH/NF.

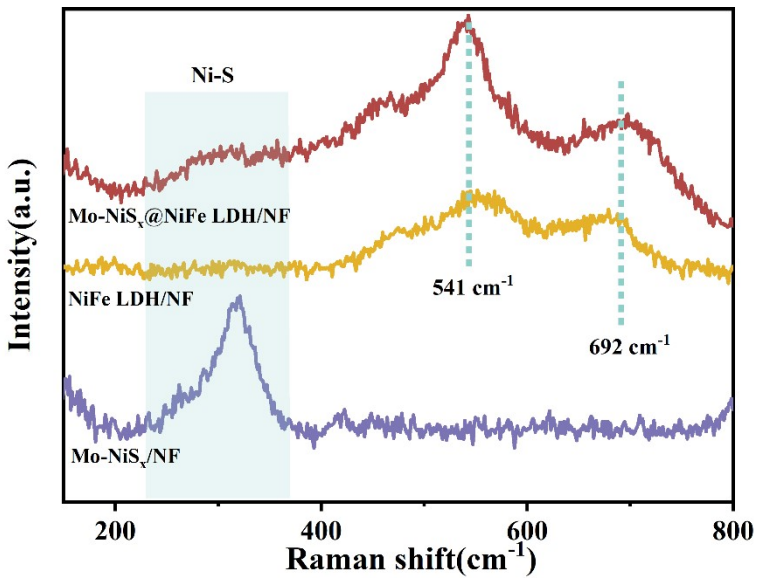

Fig. S9 Raman spectra of hydrated NiFe LDH/NF, Mo-NiS_xNF and Mo-NiS_x@NiFe LDH/NF.

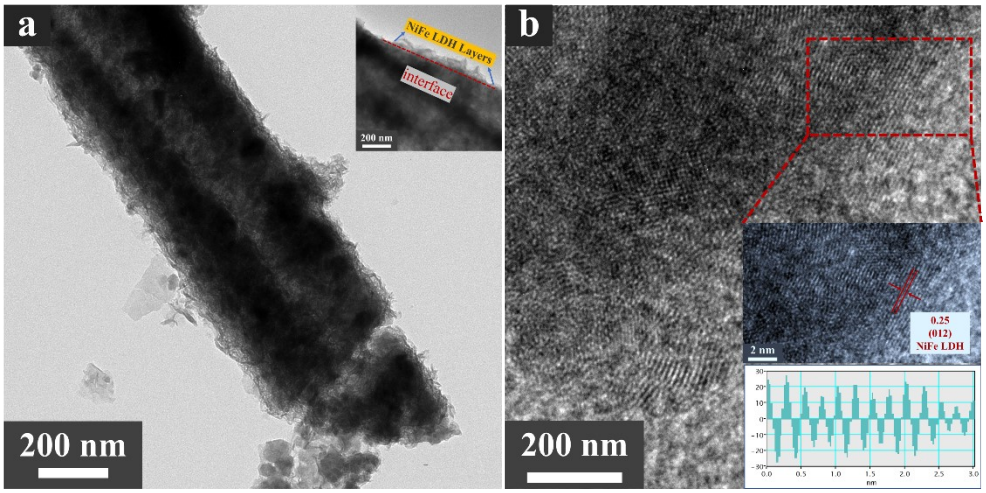

Fig. S10 a) TEM images and **b)** High-resolution TEM images of Mo-NiS_x@NiFe LDH/NF.

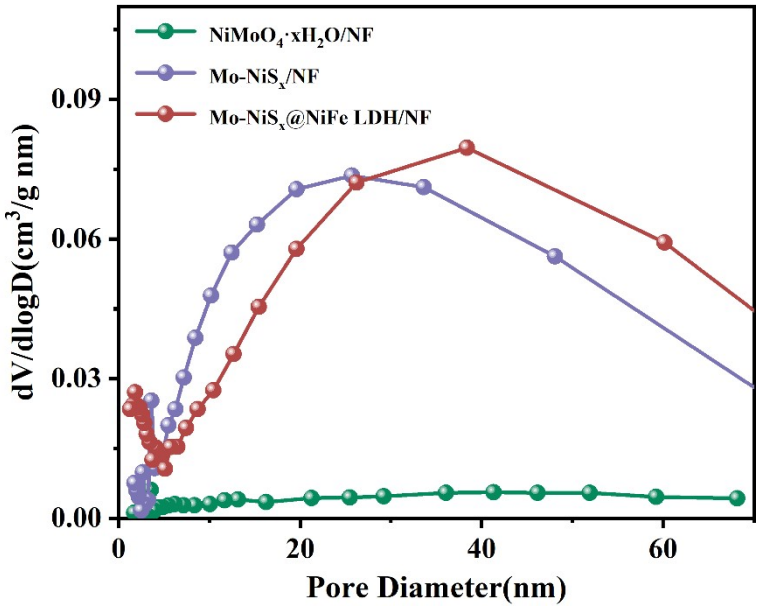

Fig. S11 Pore distribution of $NiMoO_4 \cdot xH_2O$/NF, Mo-NiS_x/NF and Mo-NiS_x@NiFe LDH/NF.

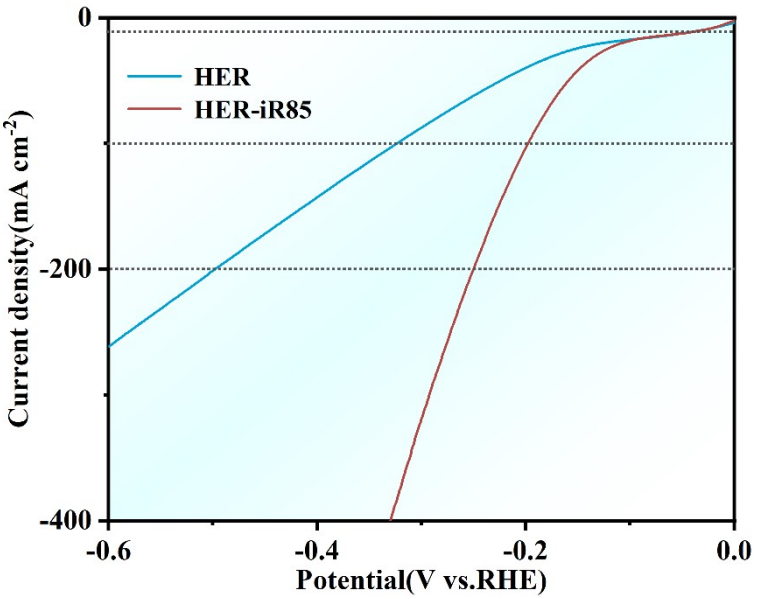

Fig. S12 HER polarization curves of Mo-NiS_x@NiFe LDH/NF with a three-electrode configuration in 1.0 M KOH.

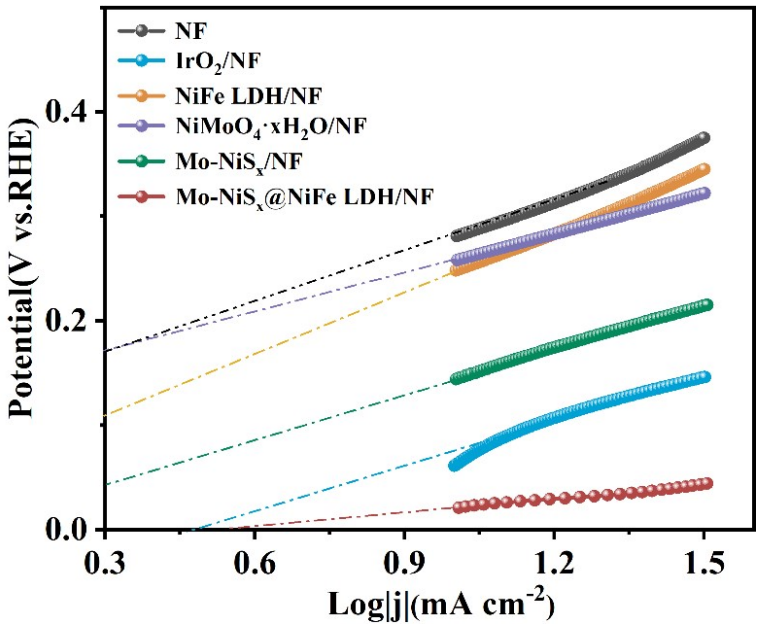

Fig. S13 Tafel plots of NF, IrO_2/NF, $NiMoO_4 \cdot xH_2O$/NF, Mo-NiS_x/NF and Mo-NiS_x@NiFe LDH/NF to calculate the exchange current density.

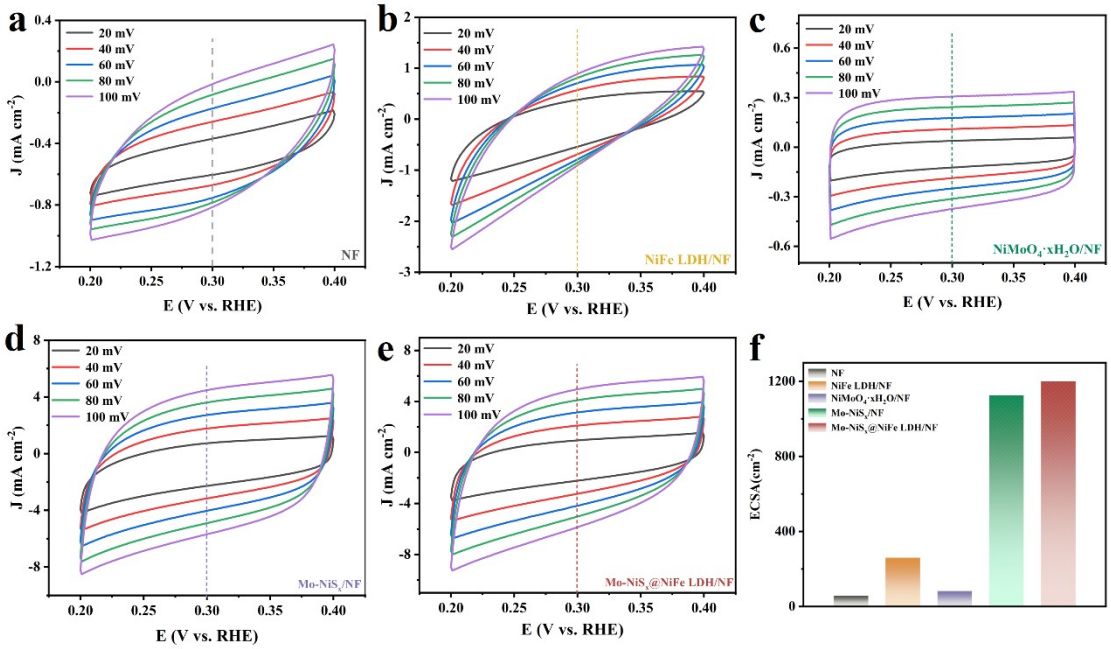

Fig. S14 CV curves of **a)** NF, **b)** NiFe LDH/NF, **c)** $NiMoO_4 \cdot xH_2O$/NF, **d)** Mo-NiS_x@NiFe LDH/NF, **e)** Mo-NiS_x@NiFe LDH/NF at varying scan rates (20-100 mV s^{-1}) and **f)** ECSA of catalysts.

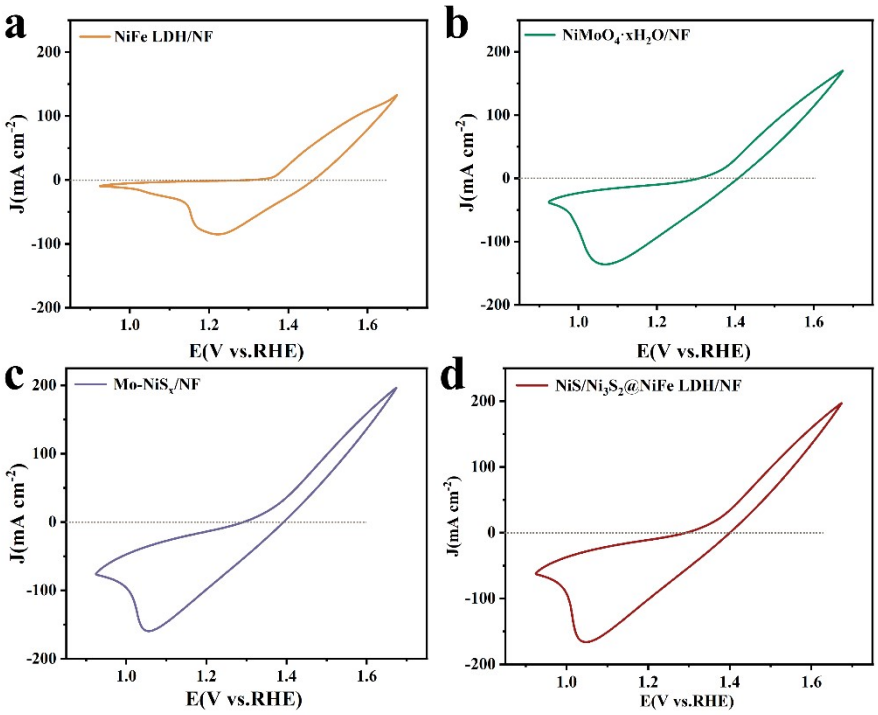

Fig. S15 Reduction peaks recorded at 0.3 V s^{-1}. **a)** NiFe LDH/NF, **b)** $NiMoO_4 \cdot xH_2O$/NF, **c)** Mo-NiS_x /NF, **d)** Mo-NiS_x@NiFe LDH/NF.

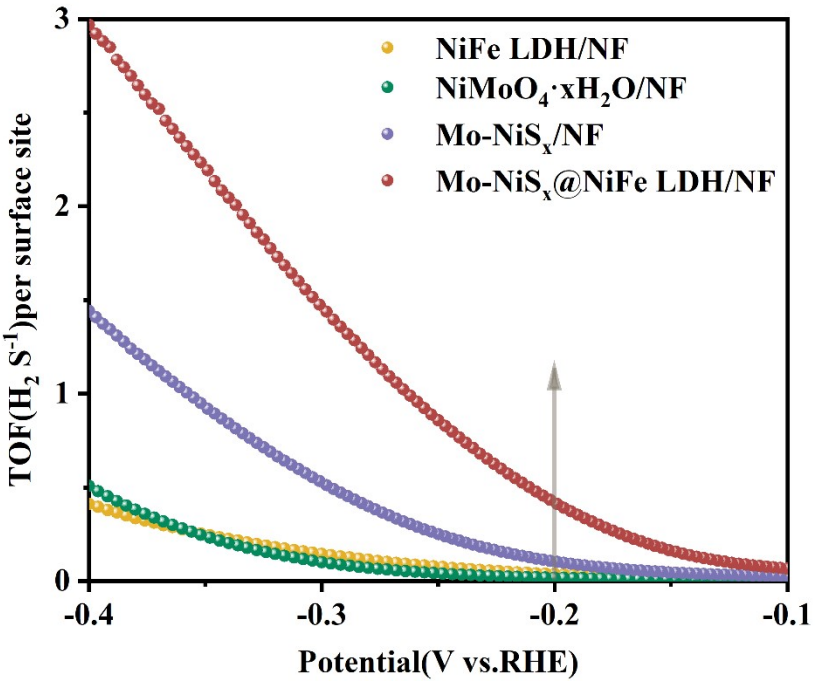

Fig. S16 The potential-dependent TOF curves of the NiFe LDH/NF, $NiMoO_4 \cdot xH_2O$/NF, Mo-NiS_x/NF, and Mo-NiS_x@NiFe LDH/NF.

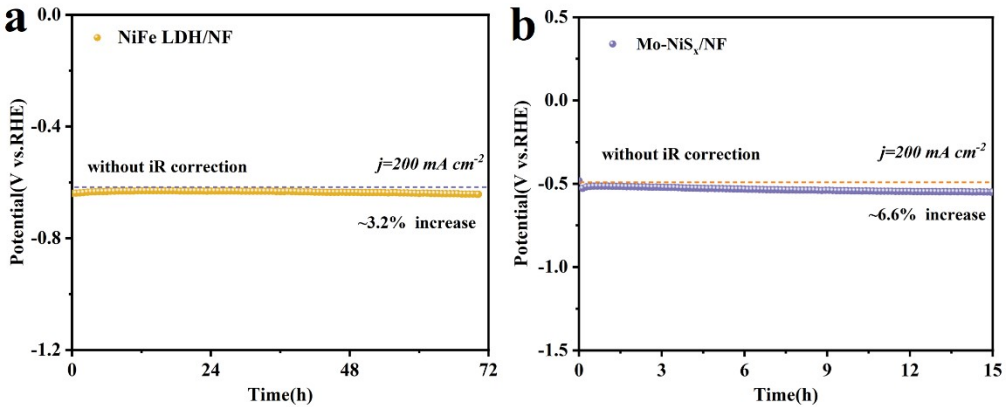

Fig. S17 The stability test of hydrogen evolution reaction with a) NiFe LDH/NF, b) Mo-NiSx/NF.

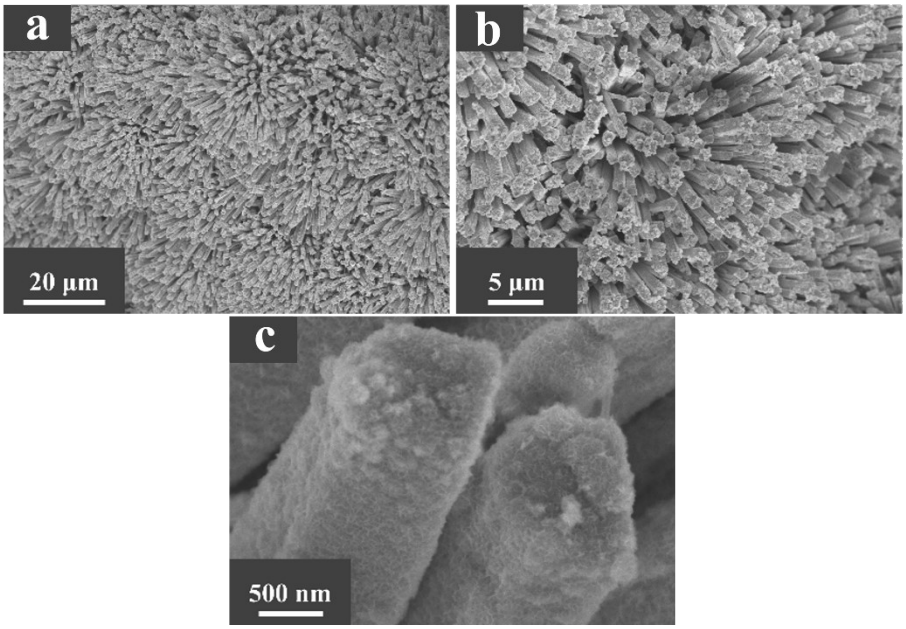

Fig. S18 SEM images of Mo-NiS_x@NiFe LDH/NF after long-term HER tests.

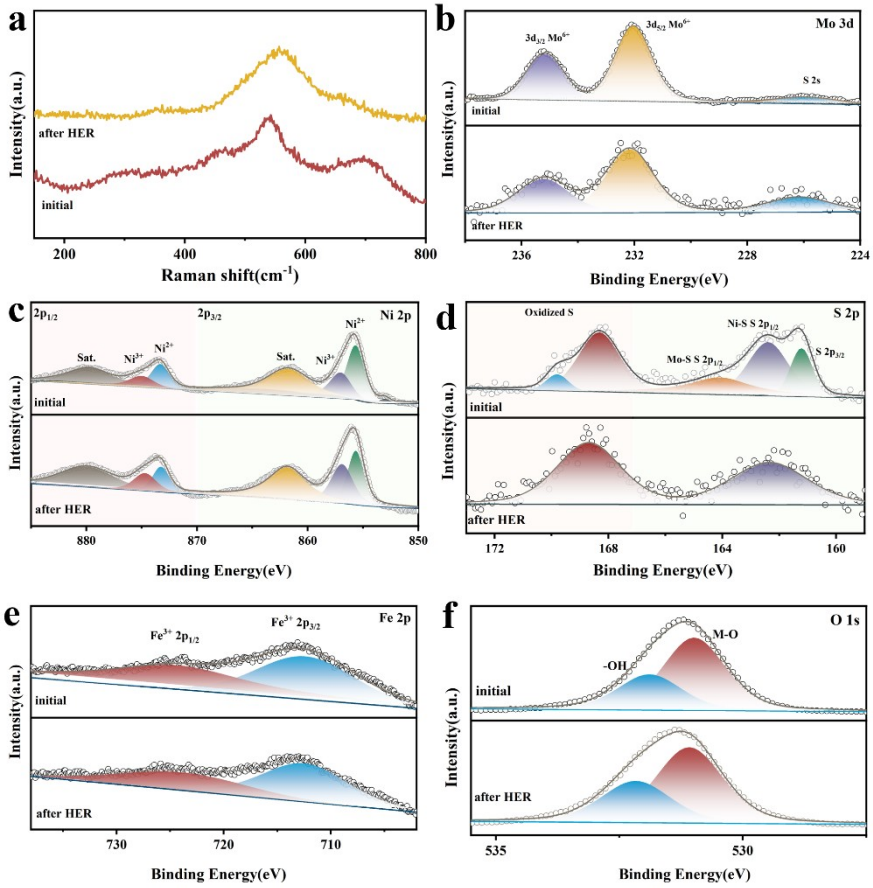

Fig. S19 a) Raman and XPS spectra of **b)** Mo 3d, **c)** Ni 2p, **d)** S 2p, **e)** Fe 2p, **f)** O 1s of Mo-NiS_x@NiFe LDH/NF after long-term HER tests.

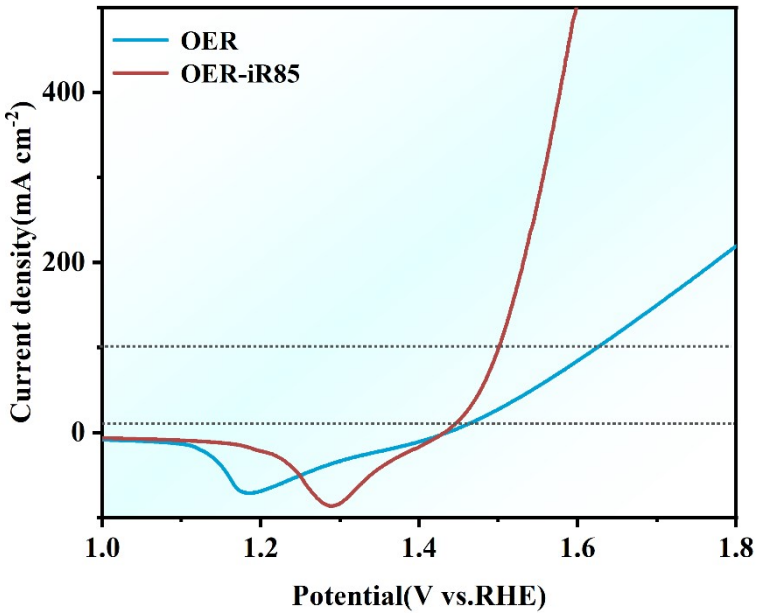

Fig. S20 OER polarization curves of Mo-NiS_x@NiFe LDH/NF with a three-electrode configuration in 1.0 M KOH.

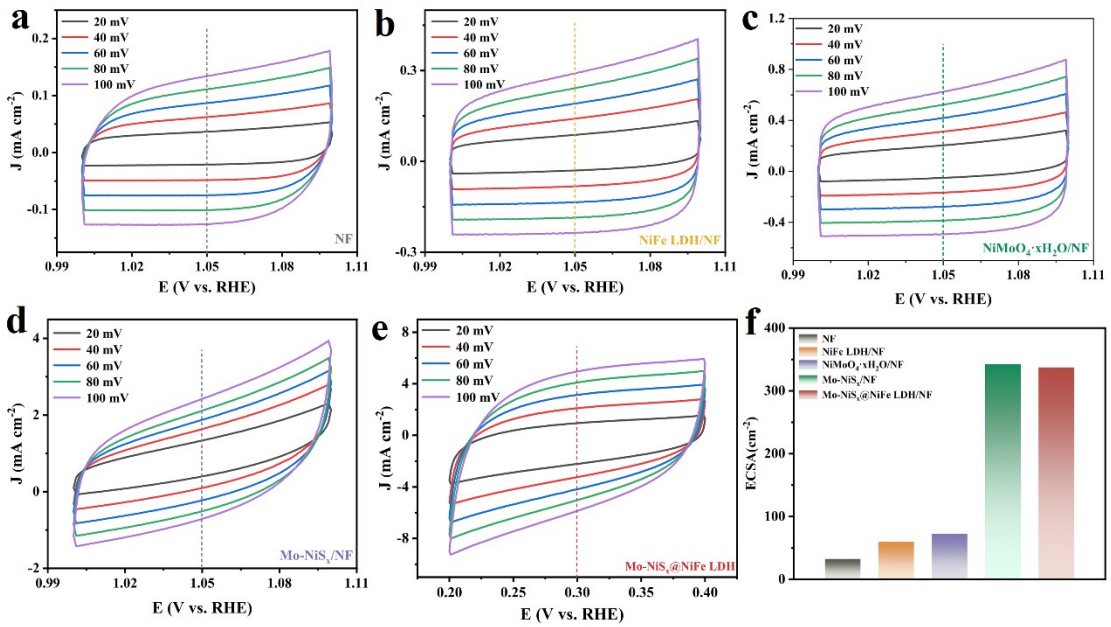

Fig. S21 CV curves of **a)** NF, **b)** NiFe LDH/NF, **c)** $NiMoO_4 \cdot xH_2O$/NF, **d)** Mo-NiSx@NiFe LDH/NF, **e)** Mo-NiS_x@NiFe LDH/NF at varying scan rates (20−100 mV s^{-1}) and **f)** ECSA of catalysts.

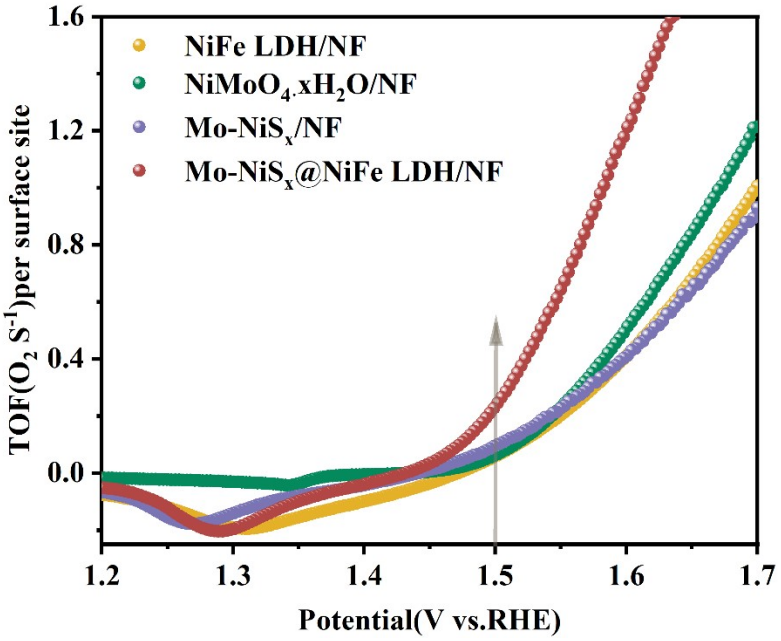

Fig. S22 The potential-dependent TOF curves of the NiFe LDH/NF, $NiMoO_4 \cdot xH_2O$/NF, Mo-NiS_x/NF, and Mo-NiS_x@NiFe LDH/NF.

Fig. S23 The stability test of oxygen evolution reaction with c) NiFe LDH/NF, d) Mo-NiSx/NF. Inset: SEM image of Mo-NiSx/NF after the OER stability test at different magnification.

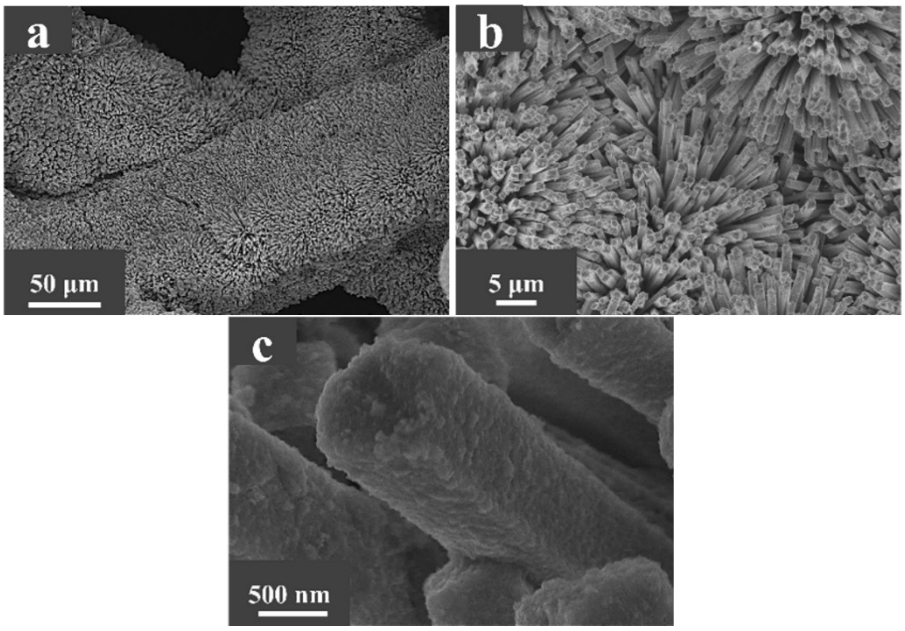

Fig. S24 SEM images of Mo-NiS_x@NiFe LDH/NF after long-term OER tests.

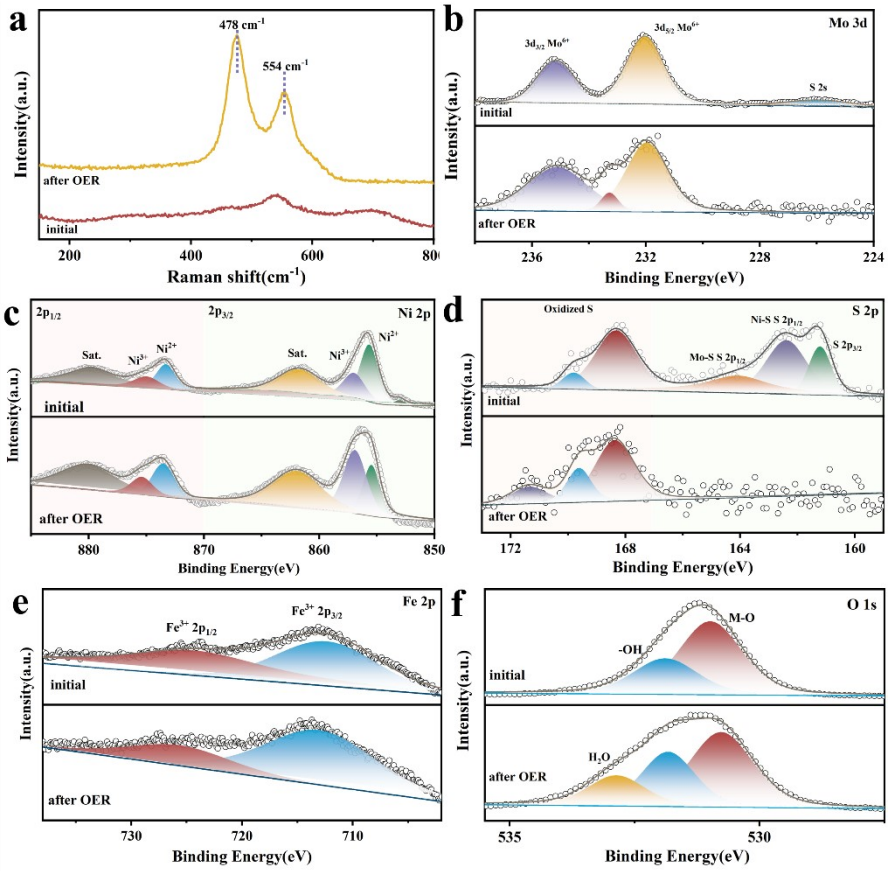

Fig. S25 a) Raman and XPS spectra of **b)** Mo 3d, **c)** Ni 2p, **d)** S 2p, **e)** Fe 2p, **f)** O 1s of Mo-NiS_x@NiFe LDH/NF after long-term OER tests.

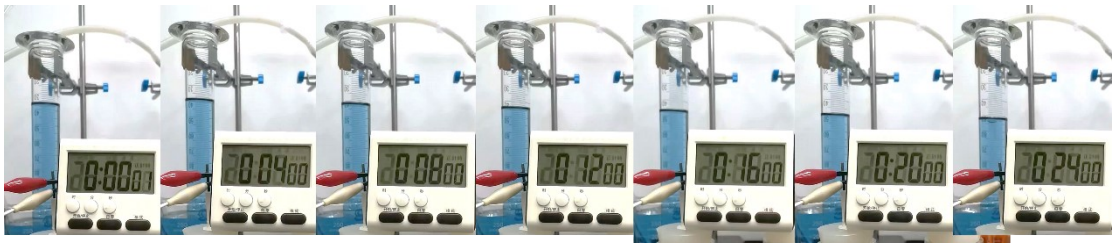

Fig. S26 Digital photograph of a drainage setup for collecting H_2 from water splitting by Mo-NiS_x@NiFe LDH/NF.

Fig. S27 Digital photograph of a drainage setup for collecting O_2 from water splitting by Mo-NiS_x@NiFe LDH/NF.

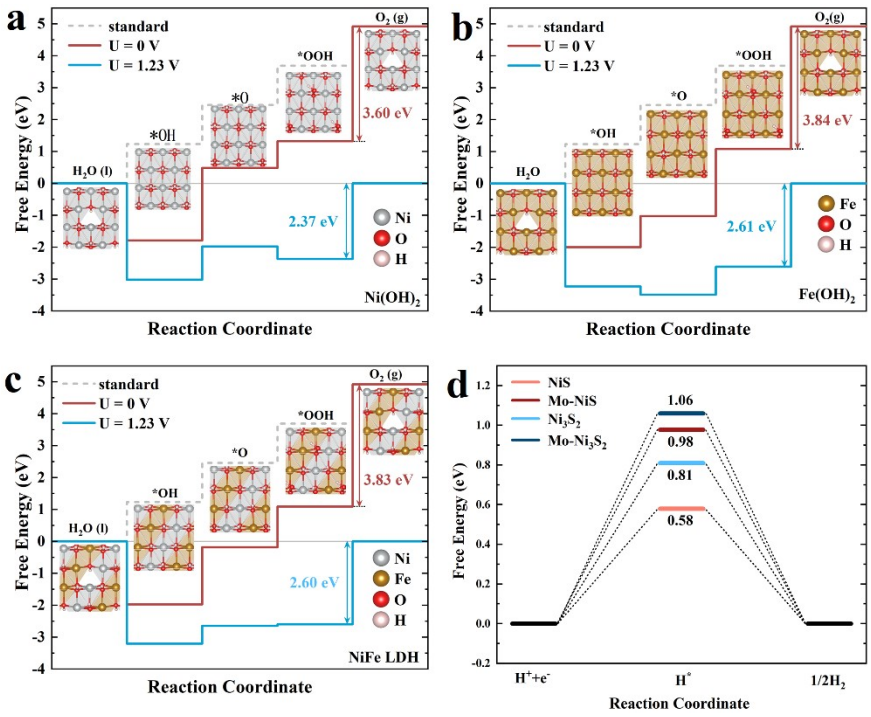

Fig. 28 Calculated OER free energy profiles of **a**) $Ni(OH)_2$, **b**) $Fe(OH)_2$ and **c**) NiFe LDH. **d**) Calculated HER free energy profiles of NiS and Ni_3S_2 surface with or without Mo-doping.

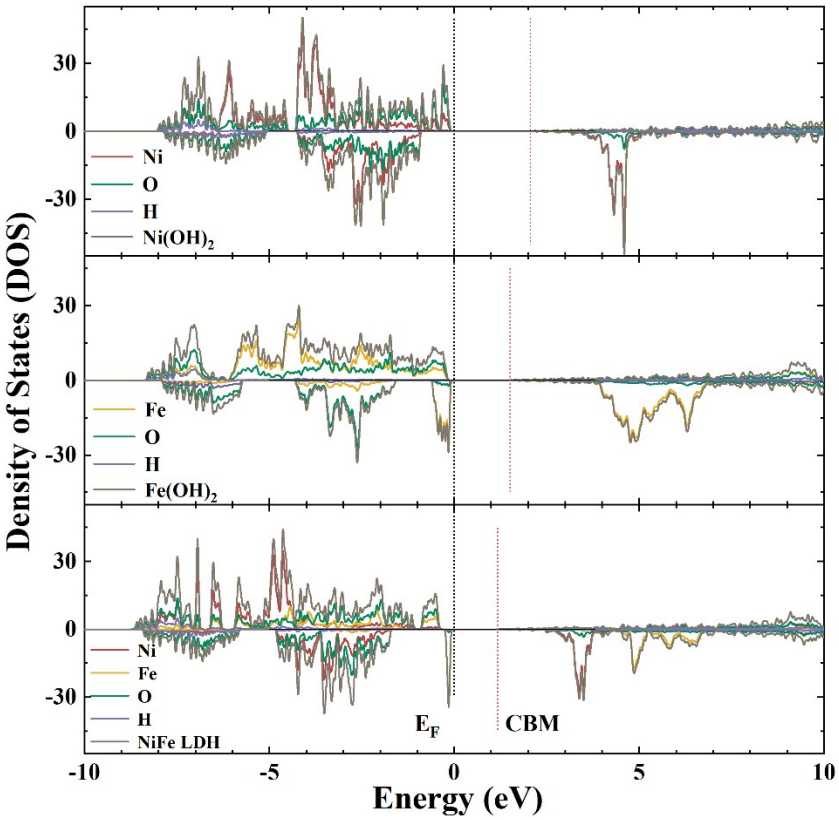

Fig. S29 Calculated DOS of $Ni(OH)_2$, $Fe(OH)_2$ and NiFe LDH.

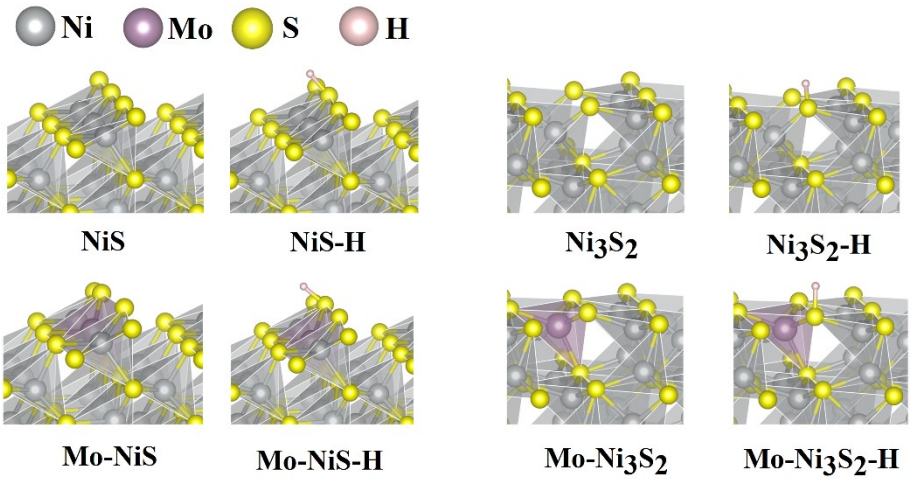

Fig. S30 Optimized surface structures of HER process on NiS and Ni_3S_2.

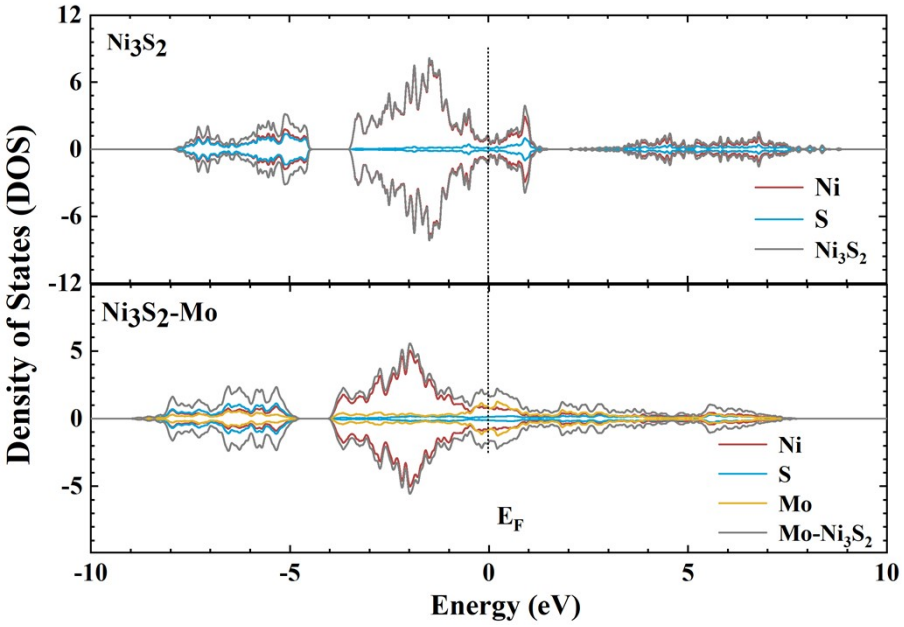

Fig. S31 Calculated DOS of Ni_3S_2 and Mo-Ni_3S_2.

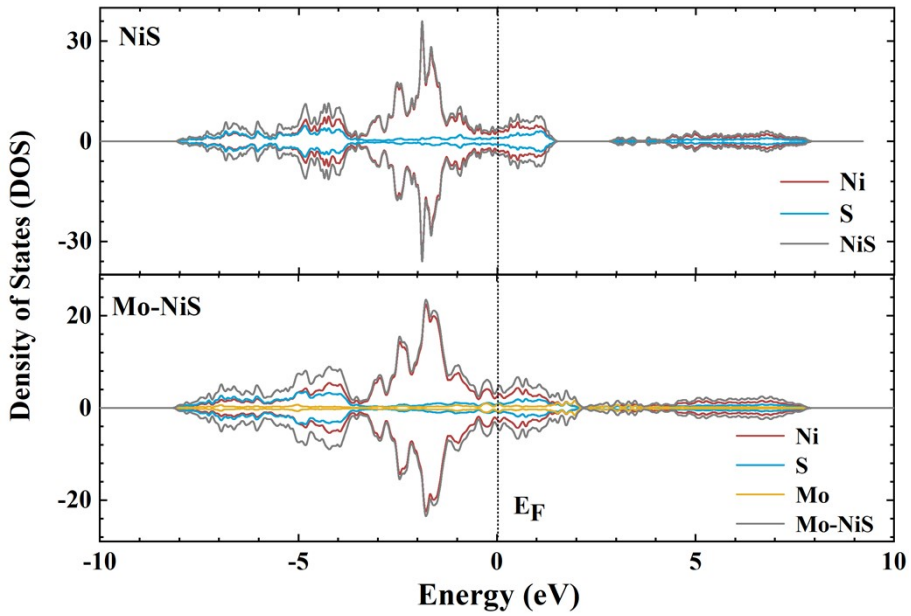

Fig. S32 Calculated DOS of NiS and Mo-NiS.

3. Appendix table

Table S1 The Rs and Rct values of of the comparison materials for HER and OER.

	HER		OER	
Electrocatalysts	R_s(Ω)	R_{ct} (Ω)	R_s (Ω)	R_{ct} (Ω)
NF	2.5	34.8	3.7	8.4
NiFe LDH/NF	3.0	13.0	3.7	2.2
$NiMoO_4 \cdot xH_2O$/NF	4.1	19.9	3.4	2.9
Mo-NiS_x/NF	3.6	4.9	3.3	2.6
Mo-NiS_x@NiFe LDH/NF	3.3	4.2	3.2	1.2

Table S2 Performance comparison of alkaline HER for non-precious S-based hydrogen evolution catalyst in 1 M KOH

Samples	10 mA cm^{-2} (mV)	Tafel slope (mV dec^{-1})	Ref.
NiFe LDH@Mo-NiS_2-NiS/NF	120	105	22
Mo-Ni_2S_3@NiFe LDH	109	86.2	23
Ni_3S_2-NiO_x	104	64	24
Ni_3S_2/VO_2	100	114	25
Co-NiOOH/Ni_3S_2@NF	87	80	26
$NiFeCoS_x$@$FeNi_3$	88	116	27
$FeWO_4$-Ni_3S_2/NF	72	54.1	28
CoS_2/MoS_2@CC	67	84	29
Co-Ni_3S_2	62	49	30
Cl-Ni_3S_2	67	84	31
Mo-NiS_x@NiFe LDH/NF	**61.3**	**26.7**	**This work**

Table S3 Performance comparison of alkaline OER for non-precious NiFe-based hydrogen evolution catalyst in 1 M KOH

Samples	100 mA cm^{-2} (mV)	Tafel slope (mV dec^{-1})	Ref.
Co-C@NiFe LDH	328	57.9	[32]
$NiFe(OH)_x$/CP	309	39	[33]
$NiFe(OH)_x$@Ni_3S_2/MoS_2-CC	312	49	[34]
Fe(20Ni)-MOF/NFF	293	39	[35]
$(Ni\text{-}Fe)S_x$/$NiFe(OH)_y$	290	58	[36]
$NiFeMoO_x$/NFF	285	48.3	[37]
MoNi/$NiMoO_x$@NiFe LDH	278	44.7	[38]
Ta-NiFe LDH	280	58.95	[39]
Mo-NiS_x@NiFe LDH/NF	**271**	**44.41**	**This work**

Table S4 Comparison of potentials at 10 mA cm^{-2} of this work with the reported bifunctional electrocatalysts in two-electrode water-splitting systems in 1.0 M KOH

electrocatalysts	J ($mA\ cm^{-2}$)	η (V)	stability (mV or mA cm^{-2}@h)	Ref.
H-CoSx@NiFe LDH/NF	10	1.59	50 mA cm^{-2}@100 h	40
Au/Ni_3S_2	10	1.52	350 mV@ 60 h	41
Ni_3Se_2@NiFe-LDH/NF	10	1.55	10 mA cm^{-2}@ 24 h	42
NF-Na-Fe-Pt	10	1.56	10 mA cm^{-2}@ 12 h	43
NiFe LDH-Ni-S/NF	10	1.56	10 mA cm^{-2}@ 20 h	44
Ag@NiFe/NF	10	1.56	10 mA cm^{-2}@ 120 h	45
$NiMo_3S_4$/CTs	10	1.55	10 mA cm^{-2}@ 72 h	46
NiFeW/CP	10	1.59	100 mA cm^{-2}@ 15 h	47
NiFe-LDH@Mo-NiS_2-NiS/NF	10	1.63	10 mA cm^{-2}@ 15 h	21
NiFe LDH@CoP/NiP_3	10	1.64	100 mA cm^{-2}@ 275 h	48
Cu_2Se@NiFe-LDHNS	10	1.67	10 mA cm^{-2}@ 40 h	49
Co-CH@NiFe-LDH/NF	10	1.46	10 mA cm^{-2}@ 200 h	2
NiFe LDH@NiCoP/NF	10	1.57	10 mA cm^{-2}@ 100 h	50
NiFe-LDH@CoS_x	10	1.6	500 mA cm^{-2}@ 20 h	51
NiFe-LDH/$Ni(OH)_2$	10	1.537	20 mA cm^{-2}@ 24 h	52
Ni-Fe-S	10	1.55	10 mA cm^{-2}@ 50 h	53
Co-Ni_3S_2	10	1.54	10 mA cm^{-2}@ 25 h	54
NF-C/CoS/NiOOH	10	1.63	20 mA cm^{-2}@ 60 h	55
Mo-NiS_x@NiFe LDH/NF	10	1.54	200 mA cm^{-2}@ 72 h	This work

4. References

1 C. Jin, P. Zhai, Y. Wei, Q. Chen, X. Wang, W. Yang, J. Xiao, Q. He, Q. Liu and Y. Gong, *Small*, 2021, **17**, 2102097-2102103.

2 S. Cao, H. Huang, K. Shi, L. Wei, N. You, X. Fan, Z. Yang and W. Zhang, *Chem. Eng. J.*, 2021, **422**, 130123-130131.

3 Y. Zhang, H. Guo, J. Ren, X. Li, W. Ren and R. Song, *Appl. Catal. B*, 2021, **298**, 120582-120593.

4 W. Kohn and L. Sham, *Phys. Rev. B*,1965, **140**, A1133-A1140.

5 P. Blöchl , *Phys. Rev. B*, 1994, **50**, 17953-17964.

6 G. Kresse and D. Joubert, *Phys. Rev. B*, 1999, **59**, 1758-1769.

7 J. Perdew and Y. Wang, *Phys. Rev. B*, 1992, **45**, 13244-13255.

8 G. Kresse and J. Hafner, *Phys. Rev. B*, 1993, **47**, 558-564.

9 L. Chen, L. Zhou, H. Lu, Y. Zhou, J. Huang, J. Wang, Y. Wang, X. Yuan and Y. Yao, *ChemComm*, 2020, **56**, 9138-9141.

10 G. Kresse and J. Furthmüller, *Phys. Rev. B*, 1996, **54**, 11169-11173.

11 G. Kresse and J. Furthmüller, *Comput. Mater. Sci.*, 1996, **6**, 15-50.

12 J. Perdew and K. Burke, *Rev. Lett.*, 1996, **77**, 3865-3874.

13 S. Grimme, J. Antony, S. Ehrlich and H. Krieg, *J. Chem. Phys.*, 2010, **132**, 154104-15411.

14 J.K. Nørskov, J. Rossmeisl, A. Logadottir, L. Lindqvist, J. Kitchin, T. Bligaard and H. Jonsson, *J. Phys. Chem. B*, 2004, **108**, 17886-17892.

15 D.R. Lide, CRC handbook of chemistry and physics, CRC press, 2004.

16 Y. Zheng, Y. Jiao, Y. Zhu, L.H. Li, Y. Han, Y. Chen, A. Du, M. Jaroniec and S. Qiao, *Nat. Commun*, 2014, **5**, 1-8.

17 J.K. Nørskov, T. Bligaard, A. Logadottir, J. Kitchin, J.G. Chen, S. Pandelov and U. Stimming, *J. Electrochem. Soc.*, 2005, **152**, J23-J30.

18 G. Solomon, A. Landström, R. Mazzaro, M. Jugovac, P. Moras, E. Cattaruzza, V. Morandi, I. Concina and A. Vomiero, *Adv. Energy Mater.*, 2021, **11**, 2101324-2101336.

19 X. Ma, C. Chang, Y. Zhang, P. Niu, X. Liu, S. Wang and L. Li, *ACS Sustain. Chem. Eng.*, 2020, **8**, 8318-8326.

20 J. Feng and Y. Yin. *Advanced Materials*, 2019, **31**, 1802349-1802363.

21 Y. Wang, Z. Guo, J. Wang, N. Yu, Y. Xue and F. Yu, *Catal. Sci. Technol.*, 2021, **11**, 7445-7453.

22 Y. Li, T. Dai, Q. Wu, X. Lang, L. Zhao and Q. Jiang, *Mater. Today Energy*, 2022, **23**, 100906-100915.

23 X. Feng, Y. Shi, J. Shi, L. Hao and Z. Hu, *Int. J. Hydrog. Energy*, 2021, **46**, 5169-5180.

24 Z. Huang, L. He, W. Zhang, W. Huang, Q. Mo, L. Yang, Q. Fu and Q. Gao, *J. Colloid Interface Sci.*, 2022, **15**, 578-589.

25 Q. Lv, L. Yang, W. Wang, S. Lu, T. Wang, L. Cao and B. Dong, *J. Mater. Chem. A*, 2019, **7**, 1196-1205.

26 Z. Wu, Y. Feng, Z. Qin, X. Han, X. Zheng, Y. Deng and W. Hu, *Small*, 2022, **XX**, 2106904-2106914.

27 J. Shen, Q. Li, W. Zhang, Z. Cai, L. Cui, X. Liu and J. Liu, *J. Mater. Chem. A*, 2022, **10**, 5442-5451.

28 Z. Wang, G. Qian, T. Yu, J. Chen, F. Shen, L. Luo, Y. Zou and S. Yin, *Chem. Eng. J.*, 2022, **XX**, 134669-134672.

29 G. Zhou, X. Wu, M. Zhao, H. Pang, L. Xu, J. Yang and Y. Tang, *ChemSusChem*, 2021, **14**, 699-708.

30 X. Tong, Y. Li, N. Pang, Y. Qu, C. Yan, D. Xiong, S. Xu, L. Wang and P. Chu, *Chem. Eng. J.*, 2021, **425**, 130455-130469.

31 W. He, H. Liu, J. Cheng, Y. Li, C. Liu, C. Chen, J. Zhao and H. Xin, *ACS Appl. Mater. Interfaces*, 2022, **14**, 6869-6875.

32 W. Li, S. Chen, M. Zhong, C. Wang and X. Lu, *Chem. Eng. J.*, 2021, **415**, 128879-128890.

33 X.H. Wang, Y. Ling, B.L. Li, X.L. Li, G. Chen, B.X. Tao, L.J. Li, N.B. Li and H. Luo, *J. Mater. Chem. A*, 2019, **7**, 2895-2900.

34 S. Wang, X. Ge, C. Lv, C. Hu, H. Guan, J. Wu, Z. Wang, X. Yang, Y. Shi and J.

Song, *Nanoscale*, 2020, **12**, 9557-9568.

35 J. Wang, Y. Jiang, C. Liu, Y. Wu, B. Liu, W. Jiang, H. Li and G. Che, *J. Colloid Interface Sci.*, 2022, **XX**, 523-537.

36 Q. Che, Q. Li, Y. Tan, X. Chen, X. Xu and Y. Chen, *Appl. Catal. B*, 2019, **246**, 337-348.

37 Y. Liu, X. Wang, Y. Zhu, H. Wang, J. Yu, H. Liu and S. Ge, *J. Colloid Interface Sci.*, 2022, **622**, 443-451.

38 Y. Wu, L. Xu, W. Xin, T. Zhang, J. Cao, B. Liu, Q. Qiang, Z. Zhou, T. Han and S. Cao, *Electrochim. Acta*, 2021, **369**, 137680-137691.

39 X. Wang, Y. Tuo, Y. Zhou, D. Wang, S. Wang and J. Zhang, *Chem. Eng. J.*, 2021, **403**, 126297-126307.

40 Y.J. Lee and S. Park, *Small*, 2022, **18**, 2200586-2200597.

41 H. Liu, J. Cheng, W. He, Y. Li, J. Mao, X. Zheng, C. Chen, C. Cui and Q. Hao, *Appl. Catal. B*, 2022, **304**, 120935-120946.

42 J. Hu, S. Zhu, Y. Liang, S. Wu, Z. Li, S. Luo and Z. Cui, *J. Colloid Interface Sci.*, 2021, **587**, 79-89.

43 Y. Zhao, Y. Gao, Z. Chen, Z. Li, T. Ma, Z. Wu and L. Wang, *Appl. Catal. B*, 2021, **297**, 120395-120406.

44 X. Zhang, Y. Xue, Q. Yan, K. Zhu, K. Ye, J. Yan, D. Cao, X. Huang and G. Wang, *Mater. Today Energy*, 2021, **21**, 100741-100752.

45 Y. Ma, D. Liu, H. Wu, M. Li, S. Ding, A.S. Hall and C. Xiao, *ACS Appl. Mater. Interfaces*, 2021, **13**, 26055-26063.

46 D. Kong, Y. Wang, S. Huang, Y. Von Lim, M. Wang, T. Xu, J. Zang, X. Li and H.. Yang, *J. Colloid Interface Sci.*, 2022, **607**, 1876-1887.

47 L. Ding, K. Li, Z. Xie, G. Yang, S. Yu, W. Wang, H. Yu, J. Baxter, H.M. Meyer, D.A. Cullen and F.Y. Zhang, *ACS Appl. Mater. Interfaces*, 2021, **13**, 20070-20080.

48 C. Song, Y. Liu, Y. Wang, S. Tang, W. Li, Q. Li, J. Zeng, L. Chen, H. Peng and Y. Lei, *Sci. China Mater.*, 2021, **64**, 1662-1670.

49 H. Qi, P. Zhang, H. Wang, Y. Cui, X. Liu, X. She, Y. Wen and T. Zhan, *J. Colloid Interface Sci.*, 2021, **599**, 370-380.

50 H. Zhang, X. Li, A. Hähnel, V. Naumann, C. Lin, S. Azimi, S.L. Schweizer, A.W. Maijenburg and R. Wehrspohn, *Adv. Funct. Mater.*, 2018, **28**, 1706847-1706856.

51 Y. Yang, Y. Xie, Z. Yu, S. Guo, M. Yuan, H. Yao, Z. Liang, Y.R. Lu, T.-S. Chan and C. Li, *Chem. Eng. J.*, 2021, **419**, 129512-129524.

52 W. Mu, D. Bao and C. Chang, *Int. J. Hydrog. Energy*, 2022, **47**, 15603-15611.

53 X.F. Yang, J. Li, X.M. Yang, C.X. Li, F. Li, B. Li and J. He, *ChemSusChem*, 2021, **14**, 3131-3138.

54 F. Wang, Y. Zhu, W. Tian, X. Lv, H. Zhang, Z. Hu, Y. Zhang, J. Ji and W. Jiang, *J. Mater. Chem. A*, 2018, **6**, 10490-10496.

55 H. Wu, Q. Lu, J. Zhang, J. Wang, X. Han, N. Zhao, W. Hu, J. Li, Y. Chen and Y. Deng, *Nanomicro Lett*, 2020, **12**, 162-174.